Nano Research

Open Access

Research Article

Graphene-skinned welded glass fiber felt for anisotropic thermal management

Xiangqi Meng[1,2,§], Jing Wu[2,§], Yawei You[2], Yulin Han[2], Chao Hu[2], Nan Liu[3] ✉, and Zhongfan Liu[1,2] ✉

[1] *College of Chemistry and Molecular Engineering, Peking University, Beijing 100091, China*
[2] *Beijing Graphene Institute, Beijing 100095, China*
[3] *Key Laboratory of Energy Conversion and Storage Materials, College of Chemistry, Beijing Normal University, Beijing 100875, China*
[§] *Xiangqi Meng and Jing Wu contributed equally to this work.*

Cite this article: *Nano Research*, **2026**, *19*, 94908609. https://doi.org/10.26599/NR.2026.94908609

ABSTRACT: Materials that can deliver in-plane heat diffusion and through-plane thermal insulation are essential for thermal management in extreme environments. However, integrating these opposing functions into a single material remains highly challenging because thermal conduction and insulation are inherently contradictory. Here, we report an anisotropic graphene-skinned welded glass fiber felt (Gr-wGFF) produced through a one-step process that couples the *in situ* growth of vertically aligned graphene nanosheets on glass fibers by plasma-enhanced chemical vapor deposition (PECVD) with the concurrent thermal welding of fiber junctions. This approach generates a continuous and covalently bonded thermal transport network at an ultralow graphene content (~0.86 wt.%), thereby overcoming the high percolation threshold commonly encountered in conventional composites. The resulting structure exhibits pronounced anisotropy: at an areal density of 430 g·m^{-2}, the Gr-wGFF achieves an in-plane thermal conductivity of 1.6 W·m^{-1}·K^{-1} and a through-plane conductivity of 0.2 W·m^{-1}·K^{-1}, corresponding to an anisotropy ratio of 8. When embedded into a phenolic resin (PR) matrix, the composite maintains high thermal anisotropy with good mechanical strength and flame retardancy. This multifunctional integration offers a solution for advanced thermal-structural applications in extreme environments.

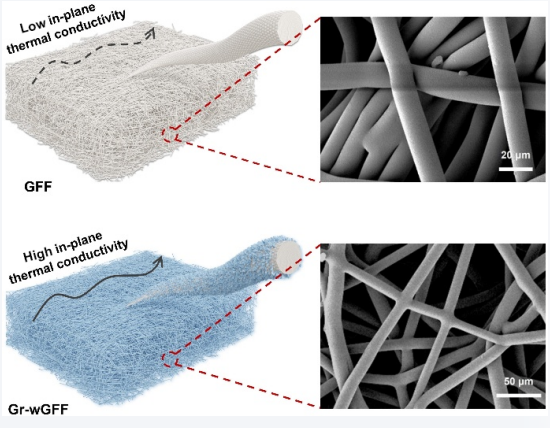

KEYWORDS: graphene-skinned welded glass fiber felt (Gr-wGFF), anisotropic thermal conductivity, plasma-enhanced chemical vapor deposition (PECVD), junction welding

1 Introduction

The effective management of extreme thermal loads is a critical challenge in high-performance engineering systems, particularly for high-speed vehicles such as rockets and missiles [1]. During flight, these vehicles are exposed to severe aerodynamic heating, which generates intense heat flux and steep thermal gradients across their outer shells. This can induce severe thermal stresses, leading to material cracking, interfacial delamination, or even catastrophic structural failure, thereby threatening vehicle safety and the operational stability of internal precision instruments [2, 3]. Consequently, an ideal thermal protection system faces a fundamental design trade-off: It must simultaneously provide through-plane thermal insulation to shield the interior from external heat and efficient in-plane heat spreading to dissipate local hot spots. However, these two functions of insulation and conduction are often mutually exclusive in conventional materials [4–6]. Therefore, developing a single, structurally robust material that reconciles these opposing thermal management requirements remains a central challenge in the field.

Glass fiber (GF) is widely used in aerospace, transportation, and other demanding applications due to its high specific strength, low density, corrosion resistance, and low cost [7–10]. In high-speed vehicles, glass fabric and glass fiber felt (GFF) are typically combined in a layered configuration [11, 12]. The outer fabric bears mechanical loads, while the inner felt reinforces resin-based composites, providing thermal insulation and buffering. This

Received: January 4, 2026; **Revised:** February 26, 2026
Accepted: February 27, 2026

✉Address correspondence to Zhongfan Liu, zfliu@pku.edu.cn; Nan Liu, nanliu@bnu.edu.cn

structure thus confers both mechanical integrity and partial thermal protection. However, GFF inherently has low thermal conductivity [13]. Its loose and porous microstructure causes poor fiber–fiber contact and high interfacial thermal resistance, which severely impede in-plane heat conduction and lead to temperature inhomogeneity and hot spots [14, 15].

A common strategy to improve the thermal conductivity of composites is to incorporate high-thermal-conductivity fillers such as graphite, carbon nanotubes, and metal particles into the matrix, but this approach faces limitations [16–19]. Uniform dispersion is difficult to achieve, and the interfacial thermal resistance between the fillers and the matrix is high [20, 21]. To form a continuous thermally conductive network, filler loadings must often exceed the percolation threshold, typically requiring over 30 vol.% [22–25]. Such high filler content not only increases the material's density but also promotes agglomeration, which impairs mechanical properties and is incompatible with the fabrication process of GFF. More importantly, this method simultaneously enhances both the in-plane thermal conductivity ($\kappa_{//}$) and through-plane thermal conductivity ($\kappa_{\perp}$) [26, 27]. This isotropic enhancement undermines the felt's intrinsic insulation and fails to deliver the anisotropic control required for effective thermal management. Therefore, it is challenging for conventional physical blending to simultaneously balance efficient in-plane (high $\kappa_{//}$) heat dissipation and effective through-plane thermal insulation (low $\kappa_{\perp}$) in GFF. In contrast, constructing a three-dimensional (3D) thermally conductive network by directly depositing a functional layer onto the fiber surfaces presents a more promising strategy. This method enables the formation of stable and continuous heat transfer pathways without altering the bulk matrix composition, thereby preserving the material's mechanical properties and processability.

To tackle these challenges, we introduce an innovative strategy. A three-dimensional, highly conductive, and interconnected thermal network is created within GFF in a single step via a synergistic process that combines plasma-enhanced chemical vapor deposition (PECVD) of a graphene skin with *in situ* high-temperature interfacial welding of the GFs. This method integrates two key functions in a single process. First, the conformal graphene layer enhances the $\kappa_{//}$ of the felt by establishing an efficient conductive network. Second, the concomitant high-temperature welding tightens the fiber–fiber contacts, significantly reducing the interfacial thermal resistance compared to that of untreated Gr-GFF, thereby ensuring excellent thermal continuity throughout the material. The resulting Gr-wGFF, modified by this synergistic treatment, exhibits remarkable anisotropic thermal conductivity. In the in-plane direction, the continuous graphene network acts as an efficient pathway for phonon transport, enabling rapid heat diffusion and temperature homogenization, which markedly mitigates the risk of hot spots. Conversely, in the through-plane direction, the inherently loose structure of the felt prevents a significant increase in thermal conductivity from the modification, thereby ensuring that its original insulation and buffering functions remain intact. This anisotropic composite addresses the conflict between heat conduction and insulation found in conventional materials. When used as a reinforcement in a phenolic resin (PR) matrix, this architecture maintains its thermal anisotropy while adding high mechanical strength, flame retardancy, and low density. This graphene-skinned welded glass fiber felt (Gr-wGFF) system offers an integrated solution for aerospace and electronics applications that require heat spreading, load-bearing, and fire safety.

2 Experimental

2.1 Preparation of Gr-wGFF

The GFF (Tianjin Tianhai Longda High-Performance Fiber Co., Ltd.) was cut into square pieces for use as substrates. Prior to graphene growth, the GFF was annealed in ambient air at 600 °C for 2 h to remove the surface resin coating. The synthesis was conducted in a three-zone tube furnace (BTF-1200C-III, AnHui BEQ Equipment Technology Co., Ltd., China). The pre-treated GFF was loaded into the central heating zone of the quartz tube. The system was first evacuated to a pressure below 30 Pa, followed by purging with high-purity argon (Ar) at a flow rate of 500 sccm. The furnace was then heated to 800–830 °C at a ramp rate of 25 °C·min^{-1} under a continuous Ar flow. Once the temperature stabilized, the chamber was evacuated again to below 30 Pa. A PECVD process was initiated by turning on the radio frequency (RF) power supply to 500 W and introducing a gas mixture of methane (CH_4, 10 sccm) and hydrogen (H_2, 40 sccm). This one-step process simultaneously achieved the *in situ* deposition of a graphene skin and the thermal welding of adjacent glass fibers. After the reaction, the system was cooled naturally to room temperature (RT) under Ar protection, yielding the Gr-wGFF.

2.2 Preparation of Gr-wGFF/PR composite

PR was mixed with acetone at a 1:1 mass ratio and stirred for 30 min to obtain a uniform solution. The GFF and Gr-wGFF were then immersed in the solution for complete infiltration. After removal, excess resin was scraped off, and the samples were pre-dried at room temperature. The prepregs were then cured in a preheated oven at 150 °C via isothermal hot-pressing for 1.5–2 h. After cooling naturally to room temperature, the resulting composites were collected.

2.3 Characterization

Raman spectra were collected on a Horiba LabRAM HR800 spectrometer using a 532 nm laser excitation source and a 50× objective lens. The morphology and microstructure were examined by scanning electron microscopy (SEM; Thermo Scientific Quattro S, 20 kV) and atomic force microscopy (AFM; Bruker Dimension Icon, ScanAsyst mode). Surface chemical composition was analyzed by X-ray photoelectron spectroscopy (XPS; Thermo Scientific Escalab Xi+). Thermal stability was evaluated by the thermogravimetric analysis (TGA; STA 449 F5). The surface temperature profiles during heating were monitored with an infrared (IR) camera (FLIR A615). The mechanical compression properties were tested using a computer-controlled electronic universal testing machine (WDW-10G, 10 kN).

2.4 Measurement of axial thermal conductivity of graphene-skinned glass fibers (Gr-GFs)

The axial thermal conductivity of an individual Gr-GF was measured using a custom-built and steady-state apparatus (Fig. S1 in the Electronic Supplementary Material (ESM)), a method selected for its superior reliability over transient techniques for fiber-like materials. During testing, a single fiber was Joule-heated by an applied current, and its resultant temperature distribution was recorded through a zinc selenide (ZnSe) window using an IR camera (FLIR A615) [28, 29]. The heat transfer along the fiber axis was modeled as a one-dimensional conduction problem, with the thermal conductivity calculated using Eq. (1)

$$-\kappa A_c \frac{d^2T}{dx^2} + hp(T_x - T_a) = \frac{UI}{2L} \quad (1)$$

where k is the thermal conductivity, A_c is the cross-sectional area of the fiber (m^2), T_x is the temperature of the fiber at position x (K), x is the axial position along the fiber (m), h is the heat transfer coefficient between the fiber and surrounding environment ($W \cdot m^{-2} \cdot K^{-1}$), p is the perimeter of the fiber cross section (m), T_a is the ambient temperature (K), U is the voltage (V), I is the current (A), and L is the half length of the suspended fiber between the center and one end (m). Under high vacuum (10^{-4} torr) with minimal temperature rise, convective and radiative heat losses become negligible, simplifying the relationship shown in Eq. (2)

$$T_x = T_a + \frac{UI}{4\kappa L A_c}(L^2 - x^2) \quad (2)$$

As the maximum temperature is located at the fiber's midpoint , the axial thermal conductivity (κ, $W \cdot m^{-1} \cdot K^{-1}$) can be derived from Eq. (3)

$$\kappa = \frac{UIL}{4A_c(T_0 - T_a)} \quad (3)$$

where T_0 is the maximum temperature at the fiber center (K).

2.5 Thermal conductivity measurement of the felts

The thermal conductivity of the GFF, Gr-GFF, Gr-wGFF, Gr-wGFF/PR, and Gr-GFF/PR was determined using Eq. (4)

$$\kappa = \alpha \times \rho \times c_p \quad (4)$$

Here, α is the thermal diffusivity ($mm^2 \cdot s^{-1}$), ρ is the bulk density ($g \cdot cm^{-3}$), and c_p is the specific heat capacity ($J \cdot g^{-1} \cdot K^{-1}$). Thermal diffusivity was measured at room temperature via the laser flash method on an LFA 467 instrument (Netzsch, Germany). Standard sample discs with diameters of 14 and 12.7 mm were used for through-plane and in-plane measurements, respectively. The specific heat capacity was obtained using differential scanning calorimetry (DSC). For accuracy, each diffusivity measurement was repeated five times.

2.6 Heat transfer simulation

COMSOL Multiphysics was used to simulate anisotropic thermal diffusion in the Gr-wGFF. The model was designed based on SEM images to reflect its key structural features. The in-plane direction was modeled as a tightly interwoven network of welded fibers, while the through-plane direction consisted of a loose and layered structure. A line heat source was applied to the top-left of the model, and a transient analysis was performed to track the heat diffusion over time in both directions.

3 Results and discussion

3.1 Synthesis of Gr-wGFF

Figure 1(a) illustrates the one-step synthesis of Gr-wGFF, in which graphene is grown *in situ* on glass fiber felt via PECVD. Graphene growth originates from the decomposition of the carbon precursor. Methane is a common carbon precursor, but its high C–H bond energy makes dehydrogenation highly endothermic. Consequently, complete decomposition of carbon precursors into reactive species typically requires temperatures approaching 1200 °C under conventional thermal processes [30]. In the PECVD process, plasma facilitates the decomposition of the carbon source, compensating for the weak catalytic activity of the glass substrate [31]. The plasma-assisted strategy enables graphene growth at a significantly lower temperature of 600–800 °C, which not only reduces energy consumption but also enhances feasibility for large-scale production. In our experiment, a GFF of 5 cm × 10 cm was placed in a tubular furnace, and plasma-assisted pyrolysis of methane was initiated at 800 °C. Under these conditions, the glass fibers soften and adjacent fibers fuse at their contact points, creating a network of welded junctions. Meanwhile, the resulting active carbon species migrate across the fiber surfaces, where they nucleate and grow into vertical graphene flakes. This vertical growth mode is characteristic of plasma-assisted decomposition under reduced temperatures, where limited surface diffusion favors out-of-plane nucleation. These flakes form coherent coatings that grow continuously along the fusing fibers, ultimately providing efficient pathways for phonon transport across the entire Gr-wGFF. By

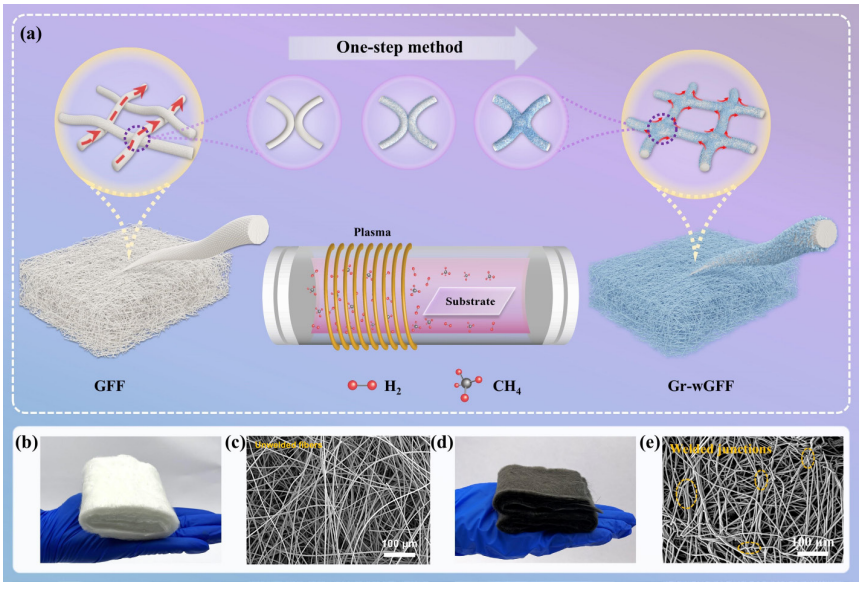

Figure 1 Synthesis of Gr-wGFF. (a) Schematic of the one-step PECVD growth of Gr-wGFF for constructing a 3D interconnected thermal conductive network. ((b) and (c)) Optical image and SEM image of pristine GFF, respectively. ((d) and (e)) Optical image and SEM image of Gr-wGFF, respectively.

comparing the optical photographs and the corresponding SEM images of GFF and Gr-wGFF before and after PECVD, thermally fused junctions are clearly observed, leading to a continuous interconnected thermal network.

3.2 Optimization of PECVD growth of Gr-GF

The introduction of the graphene skin transforms the properties of glass fibers from thermal insulators into conductors. In non-metallic solids, heat transfer is primarily mediated by lattice vibrations (phonons), and its efficiency is strongly limited by the material's crystalline integrity and defect density [32]. Therefore, precise control over the CVD growth parameters to produce high-quality graphene is essential for enhancing thermal performance. The gas flow ratio of methane-to-hydrogen (CH_4:H_2) is a critical parameter governing the structural quality of the graphene. A series of samples were prepared at CH_4:H_2 ratios ranging from 1:1 to 1:5, while keeping the deposition temperature and time constant. An increased hydrogen flow enhances the etching effect, which facilitates the removal of amorphous carbon and defects. However, an excessive hydrogen flow can also etch nascent graphene domains, thereby hindering or even halting the growth process. Raman spectroscopy was used to evaluate the structural quality and layer number of the CVD-grown graphene. The analysis focused on the G (~ 1580 cm^{-1}), D (~ 1350 cm^{-1}), and 2D (~ 2700 cm^{-1}) bands (Figs. 2(a) and 2(b)). The I_D/I_G ratio was taken as an indicator of defect density, while the shape and intensity of the 2D band were used to distinguish monolayer from multilayer graphene. The I_D/I_G ratio decreased with increasing H_2 ratio and reached its lowest value at 1:4. When the ratio increased further to 1:5, the I_D/I_G ratio rose again, indicating a higher defect density. This suggests that excessive hydrogen began to introduce new defects, thereby degrading crystalline integrity. Corroborating these findings, measurements of the axial thermal conductivity of the Gr-GF revealed a congruent trend, with the peak conductivity achieved at the 1:4 ratio (Fig. 2(c)). This independent verification confirms the CH_4:H_2 ratio of 1:4 as the optimal condition for synthesizing high-quality graphene. SEM images (Fig. 2(d)) reveal that the glass fiber surfaces are covered by a dense array of vertically aligned graphene nanosheets. Figure S2 in the ESM illustrates the morphological evolution of this dense array. The growth initiates with the nucleation of carbon species, followed by the out-of-plane growth of vertically aligned graphene nanosheets during prolonged deposition. AFM elucidated the surface topography, showing that the nanosheets have heights of approximately 200 nm (Fig. 2(e)). X-ray photoelectron spectroscopy analysis (Fig. 2(f)) confirmed the formation of the graphene skin, evidenced by a significant signal enhancement for sp^2-hybridized carbon (Fig. 2(g)). Thermogravimetric analysis indicated that the graphene skin was thermally stable up to 600 °C and constituted a mass fraction of only approximately 0.66 wt.% (Fig. 2(h)), suggesting sufficient intrinsic thermal tolerance for elevated-temperature applications. In contrast to conventional physical blending methods, the CVD process forms a continuous graphene skin *in situ* grown on the GF surfaces, thereby dramatically lowering the percolation threshold

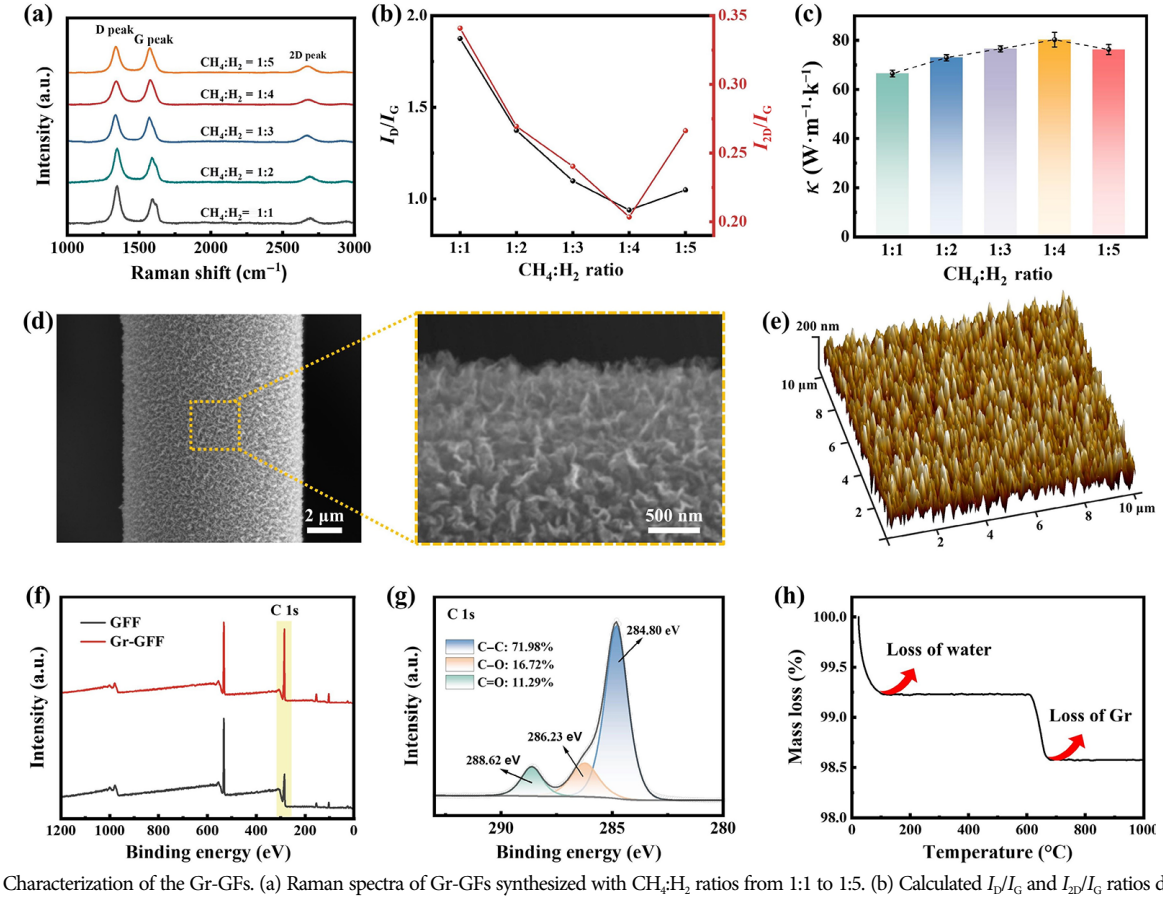

Figure 2 Characterization of the Gr-GFs. (a) Raman spectra of Gr-GFs synthesized with CH_4:H_2 ratios from 1:1 to 1:5. (b) Calculated I_D/I_G and I_{2D}/I_G ratios derived from (a). (c) Axial thermal conductivity of a single Gr-GF as a function of the CH_4:H_2 ratio. (d) SEM image of a single Gr-GF, showing a dense coating of vertically-aligned graphene nanosheets (magnified view in inset). (e) AFM image of Gr-GFs. (f) XPS survey spectra of pristine GFs and Gr-GFs. (g) High-resolution C 1s XPS spectrum of Gr-GFs. (h) TGA curve of the Gr-GFs.

for thermal conduction. Even at this exceptionally low loading, the graphene skin establishes a percolating network for efficient phonon transport, leading to a substantial enhancement in thermal conductivity.

After identifying the optimal CH_4:H_2 ratio, we investigated the effect of the number of PECVD process cycles. Raman spectroscopy reveals that the multi-cycle process not only maintains a low defect density but actively enhances the crystalline perfection of the graphene (Fig. S3 in the ESM). This is evidenced by two key trends: While the I_D/I_G ratio remains low, the I_{2D}/I_G ratio progressively increases with more cycles. This increasing I_{2D}/I_G ratio points to an improved graphitic lattice order, which is highly beneficial for phonon transport. Increasing the number of PECVD cycles resulted in taller vertically aligned graphene nanosheets. This increased nanosheet height enhanced the steric engagement between adjacent Gr-GFs, creating a strong mechanical interlocking effect within the network. Unlike planar graphene coatings that mainly cover individual fiber surfaces, the vertically aligned nanosheets protrude into the inter-fiber space. This edge-on configuration increases the real contact area at fiber junctions and strengthens mechanical interlocking between crossing fibers. As a result, phonon coupling across adjacent fibers is enhanced, which is more effective for in-plane heat transport in a felt network. These vertically aligned nanosheets outperform planar graphene films. Their larger fiber–fiber contact area provides more pathways for phonon coupling. Additionally, the interlocking architecture strengthens the interfacial adhesion between fibers. This structural enhancement directly improves the thermal performance. Figure S4 in the ESM shows that the axial thermal conductivity steadily increases as the number of deposition cycles is raised from 1 to 5. A direct comparison with commercial Toray carbon fibers revealed that, after 5 cycles of deposition, the conductivity of the graphene-skinned fibers approached the commercial benchmark.

3.3 Anisotropic thermal conduction of Gr-wGFF

The continuous graphene skin greatly enhances the axial thermal conductivity of individual Gr-GFs by providing an efficient pathway for phonon transport. However, the felt remains a loose and porous network, where numerous interfacial resistances between Gr-GFs still impose a major limitation on overall heat transport. To overcome this limitation and minimize interfacial resistance, we tuned the PECVD temperature close to the softening point of glass fibers, enabling graphene deposition on the fusing fibers. Figures 3(a) and 3(b) show SEM images of a welded junction where Gr-GFs have fused into a single entity, coated with conformal graphene skin. The corresponding energy dispersive X-ray spectroscopy (EDS, Figs. 3(c) and 3(d)) confirms the covering of graphene. In contrast to the unwelded Gr-GFF, where fibers are merely in physical contact by weak van der Waals forces, thermal welding in Gr-wGFF creates fused junctions that enable a continuous graphene network across adjacent fibers. This morphological fusion enables the graphene skin to form a single and uninterrupted layer bridging adjacent fibers, thereby establishing structural continuity of the graphene network at welded junctions. Consequently, the interfacial thermal resistance is significantly reduced, establishing a continuous and highly efficient pathway for phonon transport, as schematically illustrated in Fig. 3(e). This transition is shown in the SEM images of Figs. 3(f) and 3(g): The graphene coating on Gr-GFF exhibits clear discontinuities at the junctions, whereas on Gr-wGFF, it forms a coherent layer that seamlessly bridges the fused fibers [33–35].

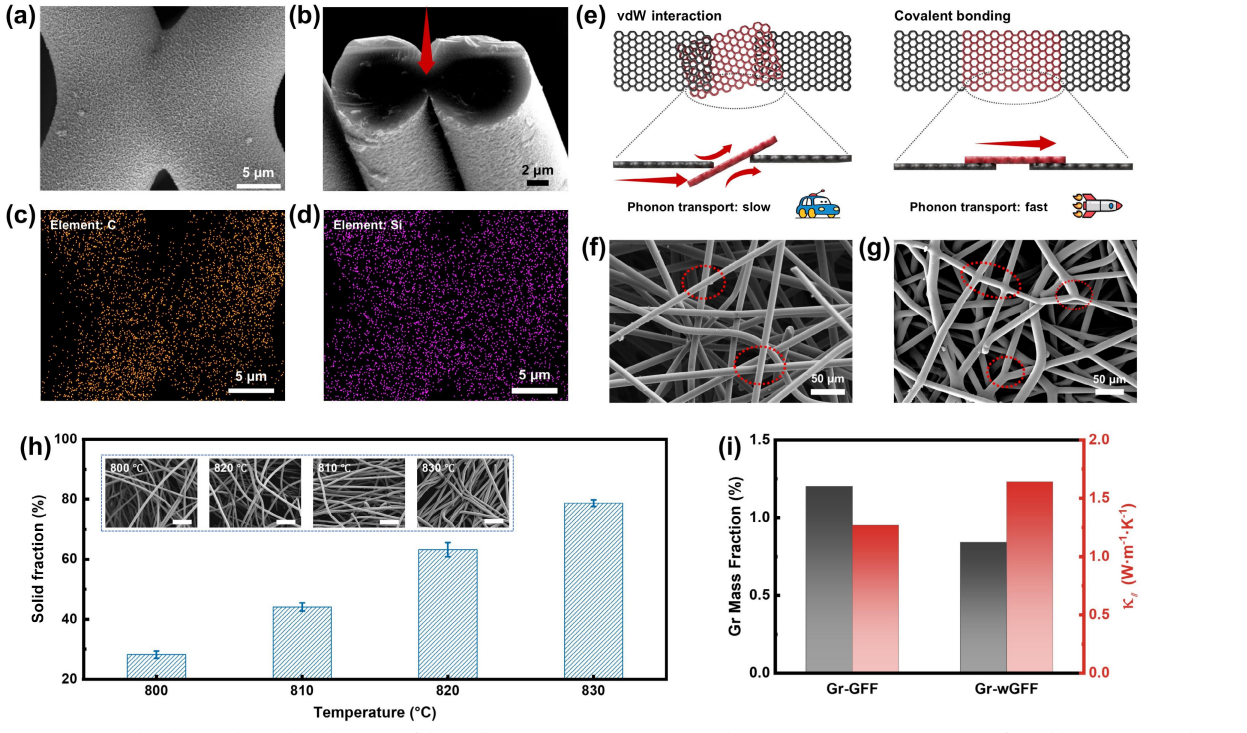

Figure 3 Microstructure and enhanced thermal conductivity of thermally Gr-wGFF. (a) Top-view and (b) cross-sectional SEM images of a welded junction in the Gr-wGFF. ((c) and (d)) EDS elemental mapping of a welded junction showing the distribution of (c) C and (d) Si. (e) Schematic comparing the graphene network connectivity and phonon transport pathways in Gr-GFF (left) and Gr-wGFF (right). ((f) and (g)) SEM images of fiber intersections in Gr-GFF and fused junctions in Gr-wGFF, respectively. (h) Effect of processing temperature on the in-plane solid volume fraction of the Gr-GFF, with SEM insets showing the morphology at corresponding temperatures. Scale bar: 100 μm. (i) Comparison of the graphene mass fraction and $\kappa_{//}$ for the unwelded Gr-GFF and Gr-wGFF.

In a fiber-felt architecture, in-plane heat transport is primarily governed by phonon transmission across fiber–fiber junctions rather than by basal-plane alignment on individual fibers. At the microscale, the conformally deposited graphene skin serves as a phonon highway that bridges adjacent fibers. On the other hand, at the macroscale, welding increases the overall density of the material. Since thermal conductivity is positively correlated with density (Eq. (4)), this densification provides an additional contribution to the enhanced thermal conductivity. Figure 3(h) compares the solid volume fraction (a direct proxy for density) of felts processed at different temperatures. The solid volume fraction was calculated by quantifying the fiber area fraction in SEM images using ImageJ, and then converting the fiber-to-air ratio into a volume fraction. As the temperature was increased from 800 to 830 °C, the solid volume fraction increased progressively. Considering the trade-off between the degree of fusion and the structural integrity of the felt, we identified 820 °C as the optimal processing temperature. At this temperature, the fibers were moderately fused in the in-plane direction, while the porous structure in the through-plane direction was largely preserved. The graphene mass fraction was determined by TGA via complete oxidation in an oxygen atmosphere, and the $\kappa_{//}$ was measured using the laser flash method. Compared to unwelded Gr-GFF, Gr-wGFF showed a lower graphene mass fraction (0.86 wt.% vs. 1.21 wt.%) but a higher $\kappa_{//}$ (1.62 vs. 1.45 $W \cdot m^{-1} \cdot K^{-1}$, Fig. 3(i)). This mass reduction results from the decreased surface area after fiber fusion, not from graphitic quality degradation. Therefore, thermal transport enhancement depends on network connectivity rather than graphene loading. In Gr-GFF, phonons must traverse two overlapping graphene layers at fiber contacts. In contrast, Gr-wGFF features a continuous graphene skin bridging the fused junctions, which minimizes interfacial scattering. This efficient network yields higher thermal conductivity even with reduced graphene content.

PECVD growth of Gr-wGFF transforms the originally insulating GFF into an anisotropic thermal conductor. As shown in Fig. 4(a), heat transfer in the through-plane direction is limited by the loosely stacked fibers. In contrast, the in-plane direction benefits from denser fiber packing, where the graphene skin and welded junctions work together to suppress interfacial thermal resistance and enable efficient phonon transport. Top-view and cross-sectional SEM images (Figs. 4(b) and 4(c)) unequivocally illustrate this structural contrast: a compact in-plane network versus a layered and porous through-plane architecture. To analyze the microscale heat transport, two-dimensional transient thermal finite element simulations were performed using COMSOL Multiphysics. The dual-phase model differentiates the solid fiber framework from the air-filled voids. The solid phase represents individual graphene-skinned glass fibers. It was assigned an intrinsic axial thermal conductivity of 120 $W \cdot m^{-1} \cdot K^{-1}$, a density of 2500 $kg \cdot m^{-3}$, and a heat capacity of 800 $J \cdot kg^{-1} \cdot K^{-1}$. The inter-fiber pores were treated as air. This void phase was set with a thermal conductivity of 0.026 $W \cdot m^{-1} \cdot K^{-1}$, a density of 1.2 $kg \cdot m^{-3}$, and a heat capacity of 1005 $J \cdot kg^{-1} \cdot K^{-1}$. The initial temperature was set to 20 °C. A constant temperature boundary of 100 °C was applied to the left (up) side as a heat source. Heat was then allowed to diffuse naturally toward the right (bottom). The results (Figs. 4(d) and 4(e)) reveal rapid and uniform heat diffusion along the in-plane interconnected fiber network. There is no obvious temperature gradient in this direction. In contrast, through-plane heat transfer is severely suppressed. This anisotropic thermal behavior strongly aligns with the material's structural features. The dense in-plane network of graphene skin and welded junctions creates efficient heat conduction pathways. Meanwhile, the loose layered through-plane structure effectively blocks heat transfer. Furthermore, we experimentally verified this disparity by measuring $\kappa_{//}$ and $\kappa_{\perp}$ of the Gr-wGFF using the laser flash method. As the areal density increased from 78 to 430 $g \cdot m^{-2}$, $\kappa_{//}$ rose markedly, while $\kappa_{\perp}$ remained largely unchanged (Fig. 4(f)). At 430 $g \cdot m^{-2}$, $\kappa_{//}$ reached 1.6 $W \cdot m^{-1} \cdot K^{-1}$, whereas $\kappa_{\perp}$ was 0.2 $W \cdot m^{-1} \cdot K^{-1}$, yielding an anisotropy ratio of 8, defined as the ratio of the in-plane to through-plane thermal conductivity ($\kappa_{//}/\kappa_{\perp}$).

The influence of deposition time was further examined (Fig. 4(g)). With prolonged PECVD duration, $\kappa_{//}$ continued to increase, whereas $\kappa_{\perp}$ remained low, confirming that phonon transport is governed primarily by the in-plane graphene network in concert with the welded junctions. To assess performance under demanding service conditions, we measured the thermal conductivity at elevated temperatures (Fig. 4(h)). For the 430 $g \cdot m^{-2}$ sample, both $\kappa_{//}$ and $\kappa_{\perp}$ increased modestly with temperature, with $\kappa_{//}$ reaching 2.06 $W \cdot m^{-1} \cdot K^{-1}$ at 300 °C. The *in situ* grown welded junctions ensure robust mechanical integrity, maintaining the structural stability of the graphene network during thermal cycling. These findings demonstrate that Gr-wGFF presents not only high $\kappa_{//}$ but also pronounced thermal anisotropy, highlighting its great potential for directional heat spreading in harsh-environment applications.

While the absolute in-plane thermal conductivity ($\kappa_{//} \approx$ 1.62 $W \cdot m^{-1} \cdot K^{-1}$) is lower than that of dense and monolithic carbon-based spreaders, the Gr-wGFF excels in specific performance (performance per unit weight) and multifunctionality. Its lightweight and porous architecture inherently provides effective through-plane thermal insulation, a feature absent in dense solid counterparts. Benchmarking against other fiber-based composites reveals that the Gr-wGFF achieves comparable in-plane heat spreading at a remarkably low filler loading (< 1 wt.%) and without energy-intensive densification. This unique integration of directional heat spreading and through-plane insulation makes it particularly attractive for aerospace applications, where minimizing mass while managing heat is critical.

3.4 Anisotropic thermal management of Gr-wGFF

To validate the anisotropic thermal management capabilities of the Gr-wGFF, we designed a unidirectional transient thermal shock experiment to evaluate its insulation, temperature homogenization, and heat dissipation performance (Fig. 5(a)). The thermal shock test was performed using a custom-built apparatus. A ceramic heater powered by a voltage source served as the heat source. An IR camera was positioned to simultaneously monitor the temperature evolution (Fig. 5(b)). The heater's temperature was calibrated against the driving voltage (Fig. S5 in the ESM). The source temperature was correspondingly defined as its steady-state value when suspended in air.

Figure 5(c) compares the thermal management performance of the materials by evaluating their cooling effect on an attached ceramic heater. When maintained at 500 °C for 200 s, the heater on bare GFF exhibited severe heat accumulation due to the material's low thermal conductivity, resulting in a hot-spot temperature rise to 520 °C. In contrast, the graphene coating on the Gr-GFF enabled lateral heat spreading, which slightly reduced the heater's maximum temperature to 502 °C. The Gr-wGFF showed the most pronounced improvement: Its integrated graphene network and

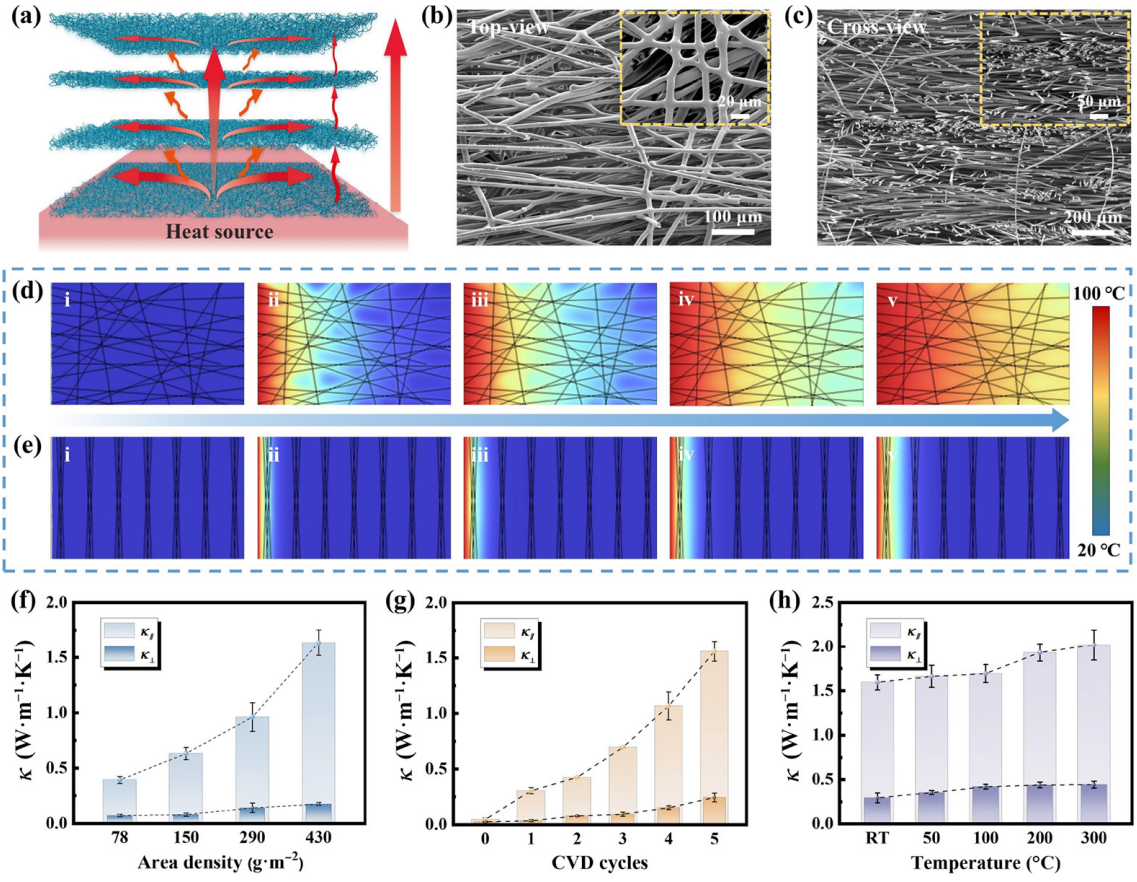

Figure 4 Anisotropic thermal conductivity of Gr-wGFF. (a) Schematic illustrating the anisotropic structure and the corresponding heat transport in the in-plane and through-plane directions. ((b) and (c)) Top-view and cross-view SEM images of Gr-wGFF, with insets showing magnified views. ((d) and (e)) COMSOL simulation of heat diffusion in (d) the in-plane and (e) through-plane directions. (f) $\kappa_{//}$ and $\kappa_{\perp}$ values as a function of areal density. (g) $\kappa_{//}$ and $\kappa_{\perp}$ values as a function of CVD cycles. (h) $\kappa_{//}$ and $\kappa_{\perp}$ values as a function of temperature.

welded fiber interface facilitated efficient lateral heat conduction, further lowering the heater's peak temperature to 482 °C. This corresponds to a reduction of 38 °C compared to the GFF case, demonstrating a clear transition from heat accumulation to active dissipation. The infrared thermographic images in Fig. 5(d) provide visual confirmation of this trend. The GFF sample shows a localized hot zone, whereas the Gr-wGFF exhibits a more uniform and cooler temperature distribution under the same electrical input, corroborating its enhanced heat-spreading capability. Additionally, Fig. S6 in the ESM summarizes the thermal management performance across a broader range of heater temperatures (100–400 °C), further underscoring the advantage of Gr-wGFF. This cooling effect is due to the material's ability to spread heat across its surface. Figures 5(e) and 5(f) show the in-plane temperature distribution from IR imaging. The GFF surface shows a concentrated hot spot, while the Gr-wGFF surface has a more uniform temperature distribution. This indicates a synergy between the welding and the graphene: The thermal weld allows heat to transfer to the graphene skin, which then diffuses the heat in-plane.

The thermal insulation performance was evaluated using the setup shown in Fig. 5(g), where a ceramic heater was fixed to the bottom surface of the sample and an IR camera monitored the top surface temperature. The results (Fig. 5(h)) show that when the heater reached 500 °C, the top surface temperature increased from 241 °C for the GFF to 250 °C for the unwelded Gr-GFF, and further to 263 °C for the Gr-wGFF. Although this trend indicates a slight decrease in insulation performance due to the enhanced $\kappa_{\perp}$, the top surface temperatures of all samples still remained much lower than that of the heat source. The IR image of the sample in Fig. 5(i) clearly shows the temperature distribution across the cross-section. These results demonstrate that Gr-wGFF retains the core through-plane insulation capability of the felt matrix while enabling efficient in-plane heat spreading. This synergy achieves a well-managed balance between effective insulation and lateral dissipation, highlighting the material's versatile and anisotropic thermal management capabilities.

3.5 Integrated study of multifunctional properties of Gr-wGFF/PR

To further evaluate its potential for the outer shells of high-speed vehicles, we impregnated PR into the aforementioned fiber felt and investigated the anisotropic thermal, mechanical, and flame-retardant properties (Fig. 6(a)). As observed in the top-view (Fig. 6(b)) and cross-sectional (Fig. 6(c)) images, the PR uniformly infiltrates and seamlessly encapsulates the Gr-wGFF. The three-dimensional network structure formed by fusion welding is retained due to the strong interfacial bonding between fibers.

The in-plane thermal conductivity of the Gr-wGFF/PR composite is higher than that of the Gr-GFF/PR composite at both 25 and 300 °C (Fig. 6(d)), which is attributed to the stable thermal bridging network formed by graphene at the welded fiber junctions. The in-plane to through-plane thermal conductivity ratio of the Gr-

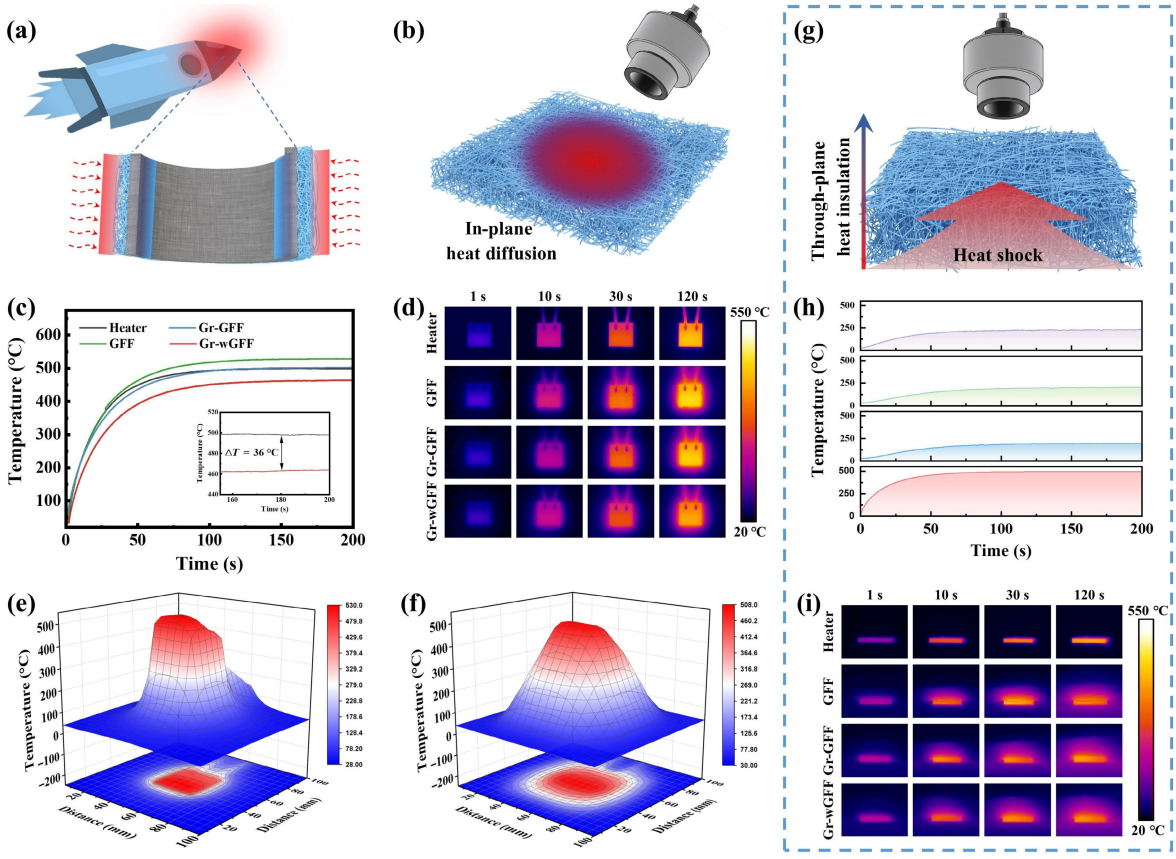

Figure 5 Anisotropic thermal management of Gr-wGFF. (a) Schematic of the thermal challenges for the outer shell of a high-speed vehicle. (b) Schematic of the test setup for evaluating in-plane heat dissipation and temperature homogenization. (c) Heater surface temperature versus time for the GFF, Gr-GFF, and Gr-wGFF. (d) Corresponding IR thermographic images of the heater surface at selected time points. ((e) and (f)) Surface temperature distribution maps of (e) the pristine GFF and (f) Gr-wGFF after applying 14 V for 200 s. (g) Schematic of the test setup for evaluating through-plane thermal insulation. (h) Top surface temperature of the samples versus time. (i) Corresponding IR thermographic images of the samples' top surfaces at selected time points.

wGFF/PR composite reaches 9.1 at 25 °C, significantly exceeding the value of 1.8 for the Gr-GFF/PR composite (Fig. 6(e)). This ratio is even slightly higher than that of the pristine Gr-wGFF material before resin impregnation (~ 8). Although the replacement of air with PR caused a slight increase in the through-plane thermal conductivity, the in-plane thermal conductivity exhibited a much more significant enhancement. This dominant in-plane improvement is attributed to the compaction of the fiber network by capillary contraction forces during PR curing, which optimizes the graphene-based heat conduction pathways. Consequently, the anisotropy ratio increased from 8 to 9.1. In the compressive stress–strain curves (Fig. 6(f)), the compressive strength of the Gr-wGFF/PR composite at 65% strain shows a reduction of 16.8% compared to that of the Gr-GFF/PR composite. This minor mechanical trade-off is accompanied by a remarkable increase in the anisotropic thermal conductivity ratio (from 1.8 to 9.1), achieving the key functionality of efficient in-plane heat conduction coupled with effective through-plane thermal insulation. In the flame-retardant test shown in Fig. 6(g), no rapid burning occurred within 5 s after ignition. At 25 s, red embers appeared on the surface, and after 35 s the burned area expanded. The heated region did not collapse, shrink, or lose material; instead, it transformed into a white residue. This observation indicates that the composite effectively suppresses flame propagation and exhibits flame-retardant performance. Figure 6(h) demonstrates the lightweight characteristics of the Gr-wGFF/PR composite.

4 Conclusions

In summary, we developed a Gr-wGFF via plasma-enhanced chemical vapor deposition. Conformal graphene skins and fused fiber junctions form continuous phonon pathways for efficient in-plane heat transport, while heat conduction across the thickness is effectively suppressed. The Gr-wGFF shows an anisotropy ratio of 8, with an in-plane thermal conductivity of 1.6 $W \cdot m^{-1} \cdot K^{-1}$ and a low through-plane thermal conductivity of 0.2 $W \cdot m^{-1} \cdot K^{-1}$. When integrated into a phenolic resin matrix, the composite retains a high thermal anisotropy ratio of 9.1 while providing excellent mechanical property and flame retardancy. This material system offers a practical solution for thermal-structural applications in aerospace and high-power electronics under extreme environments.

Electronic Supplementary Material: Supplementary material (additional characterization results and Figs. S1–S6) is available in the online version of this article at https://doi.org/10.26599/NR.2026.94908609.

Data availability

All data needed to support the conclusions in the paper are presented in the manuscript and the Electronic Supplementary Material. Additional data related to this paper may be requested from the corresponding author upon request.

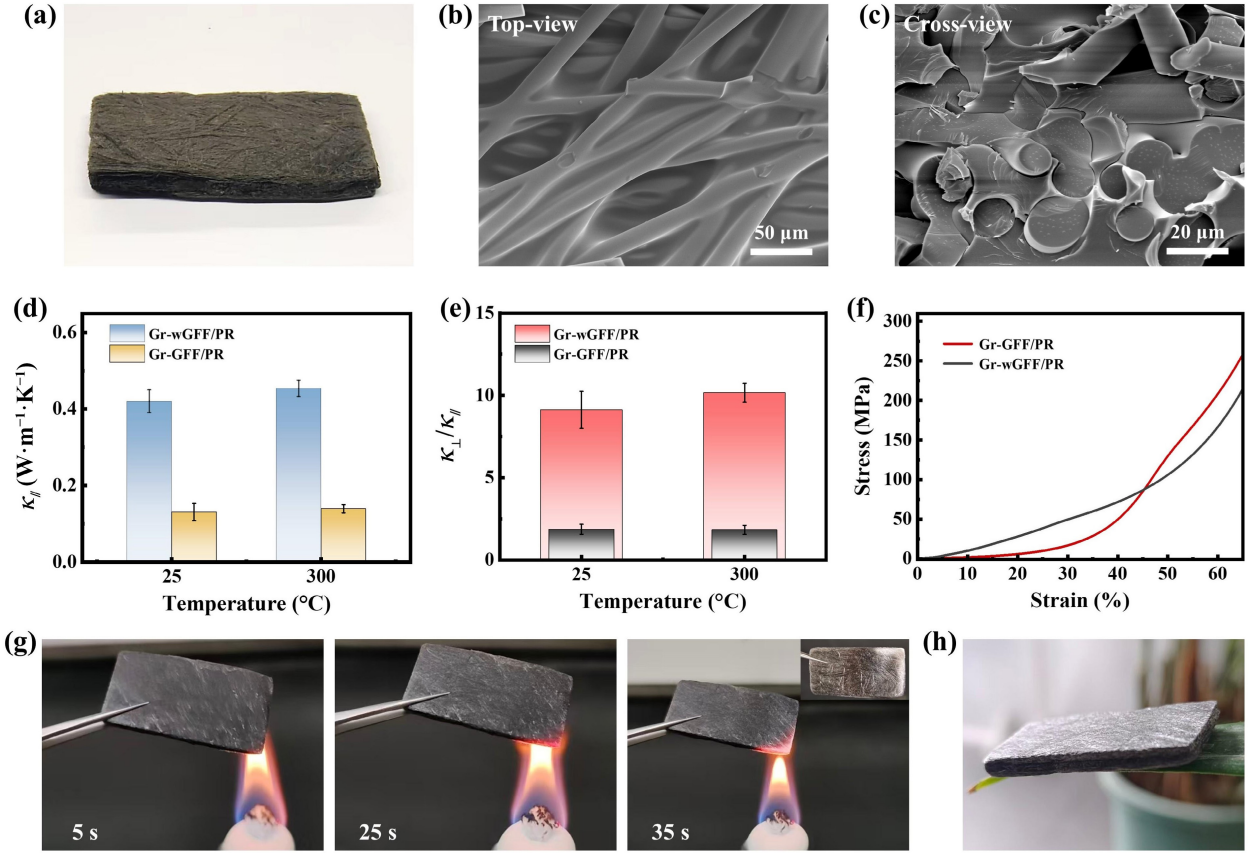

Figure 6 Anisotropic thermal, mechanical, and flame-retardant properties of Gr-wGFF/PR composite. (a) Optical image of Gr-wGFF/PR composite material. (b) Top-view and (c) cross-sectional SEM images of the composite. (d) In-plane thermal conductivity of the Gr-wGFF/PR and Gr-GFF/PR composites at 25 and 300 °C. (e) Ratios of in-plane to through-plane thermal conductivity for the Gr-wGFF/PR and Gr-GFF/PR composites at 25 and 300 °C. (f) Compressive stress–strain curves of the Gr-wGFF/PR and Gr-GFF/PR composites. (g) Optical images of the Gr-wGFF/PR composite during combustion. (h) Photo of Gr-WGFF/PR composite on an aloe vera leaf, demonstrating its lightweight nature.

Acknowledgements

Financial support for this study is gratefully acknowledged, including the National Natural Science Foundation of China (Nos. T2188101 and 22275022), Beijing National Laboratory for Molecular Sciences (No. BNLMS-CXTD-202001), the Beijing Natural Science Foundation (Nos. Z240025 and JQ23002), and the National Key Research and Development Program of China (No. 2024YFF0509300).

Declaration of competing interest

All the contributing authors report no conflict of interests in this work. Author Zhongfan Liu is the advisory board member of this journal, but he is not involved in the peer-review or decision of this article.

Author contribution statement

X. Q. M.: Investigation, formal analysis, writing – original draft. J. W.: Investigation, formal analysis. Y. W. Y.: Software, validation. Y. L. H.: Conceptualization, methodology. C. H.: Conceptualization, methodology. N. L.: Supervision, writing – review & editing. Z. F. L.: Supervision, funding acquisition, resources, project administration. All the authors have approved the final manuscript.

Use of AI statement

During the preparation of this work, the authors used Chatgpt and Gemini in order to proofread English grammar and polish language in specific sections. After using this tool/service, the authors reviewed and edited the content as needed and take full responsibility for the content of the publication.

References

[1] Peters, A. B.; Zhang, D. J.; Chen, S.; Ott, C.; Oses, C.; Curtarolo, S.; McCue, I.; Pollock, T. M.; Eswarappa Prameela, S. Materials design for hypersonics. *Nat. Commun.* **2024**, *15*, 3328.

[2] Wang, X. Q.; Tao, Y. Q.; Zhou, N.; Luo, X. G.; Ma, B.; Xu, B. S. SiBCN-ZrO_2 aerogel-modified carbon-bonded carbon fiber composite with enhancement of in-plane thermal conductivity for thermal protection applications. *Chem. Eng. J.* **2025**, *519*, 165426.

[3] Yang, Y. Z.; Yang, J. L.; Fang, D. N. Research progress on thermal protection materials and structures of hypersonic vehicles. *Appl. Math. Mech.* **2008**, *29*, 51–60.

[4] Hu, J. K.; Feng, D. L.; Li, W. J.; Miao, J. Y.; Feng, Y. H. Constructing hierarchical porous SiC/SiO_2 ceramics-based phase change composites with low thermal conductivity and high strength for aircraft thermal protection. *Ceram. Int.* **2025**, *51*, 12408–12419.

[5] Wang, Y. P.; Chen, Z. F.; Yang, L. X.; Ai, S. F.; Zhang, J. X.; He, L. H.; Li, M. N. Macroscale fabrication of lightweight, strong and insulation melamine-derived carbon foam through hot pressing followed by pyrolysis. *Chem. Eng. J.* **2025**, *518*, 164587.

[6] Yuan, C.; Lü, X. Z.; Bao, W. M. Thermal protection performance of biomimetic flexible skin for deformable high-speed vehicles (DHSV-Bio-FS) under uniaxial tensile strain. *Research* **2024**, *7*, 0394.
[7] Patil, S. P.; Shendye, P.; Markert, B. Molecular dynamics simulations of silica aerogel nanocomposites reinforced by glass fibers, graphene sheets and carbon nanotubes: A comparison study on mechanical properties. *Compos. B: Eng.* **2020**, *190*, 107884.
[8] Zhang, J. Z.; Xu, S.; Fan, J. S.; Wang, K.; Huang, J.; Wang, J. H.; Zhang, S. L.; Tao, G. M.; Zhang, Z. J. Surface coatings of glass fiber: Exploring emerging functionalities and beyond. *Adv. Fiber Mater.* **2025**, *7*, 1731–1765.
[9] Liu, Y. D.; Jiang, D. W.; Hessien, M. M.; Mahmoud, M. H. H.; Xu, M. J.; El-Bahy, Z. M. Enhanced thermal and mechanical properties of boron-modified phenolic resin composites with multifiller system for aerospace applications. *Adv. Compos. Hybrid Mater.* **2024**, *7*, 180.
[10] Sim, J. H.; Yu, S. H.; Yoon, H. S.; Kwon, D. J.; Lee, D. H.; Bae, J. S. Characteristic evaluation and finite element analysis of glass fiber/recycled polyester thermoplastic composites by cross-sectional shape of glass fiber. *Compos. B: Eng.* **2021**, *223*, 109095.
[11] Elmahdy, A.; Verleysen, P. Mechanical behavior of basalt and glass textile composites at high strain rates: A comparison. *Polym. Test.* **2020**, *81*, 106224.
[12] Wallenberger, F. T.; Brown, S. D. High-modulus glass fibers for new transportation and infrastructure composites and new infrared uses. *Compos. Sci. Technol.* **1994**, *51*, 243–263.
[13] Chen, F.; Xiao, H.; Peng, Z. Q.; Zhang, Z. P.; Rong, M. Z.; Zhang, M. Q. Thermally conductive glass fiber reinforced epoxy composites with intrinsic self-healing capability. *Adv. Compos. Hybrid Mater.* **2021**, *4*, 1048–1058.
[14] Fu, X. T.; Si, L. M.; Zhang, Z. X.; Yang, T. T.; Feng, Q. C.; Song, J. W.; Zhu, S. Z.; Ye, D. D. Gradient all-nanostructured aerogel fibers for enhanced thermal insulation and mechanical properties. *Nat. Commun.* **2025**, *16*, 2357.
[15] Jiang, Z.; Ouyang, T.; Ding, L.; Li, W.; Li, W. W.; Balogun, M. S. 3D self-bonded porous graphite fiber monolith for phase change material composite with high thermal conductivity. *Chem. Eng. J.* **2022**, *438*, 135496.
[16] Ouyang, Y. X.; Qiu, L.; Zhang, X. H.; Feng, Y. H. Modulating heat transport inside cnt assemblies: Multi-level optimization and structural synergy. *Carbon* **2023**, *205*, 236–252.
[17] Krings, E. J.; Zhang, H. P.; Sarin, S.; Shield, J. E.; Ryu, S.; Markvicka, E. J. Lightweight, thermally conductive liquid metal elastomer composite with independently controllable thermal conductivity and density. *Small* **2021**, *17*, 2104762.
[18] Yang, X. M.; Li, C. B.; Ma, Y. F.; Chi, H.; Hu, Z. J.; Xie, J. F. High thermal conductivity of porous graphite/paraffin composite phase change material with 3D porous graphite foam. *Chem. Eng. J.* **2023**, *473*, 145364.
[19] Ji, S. Y.; Jung, H. B.; Kim, M. K.; Lim, J. H.; Kim, J. Y.; Ryu, J.; Jeong, D. Y. Enhanced energy storage performance of polymer/ceramic/metal composites by increase of thermal conductivity and coulomb-blockade effect. *ACS Appl. Mater. Interfaces* **2021**, *13*, 27343–27352.
[20] Fu, C. J.; Li, Q.; Lu, J. B.; Mateti, S.; Cai, Q. R.; Zeng, X. L.; Du, G. P.; Sun, R.; Chen, Y.; Xu, J. B. et al. Improving thermal conductivity of polymer composites by reducing interfacial thermal resistance between boron nitride nanotubes. *Compos. Sci. Technol.* **2018**, *165*, 322–330.
[21] Ren, L. L.; Li, Q.; Lu, J. B.; Zeng, X. L.; Sun, R.; Wu, J. B.; Xu, J. B.; Wong, C. P. Enhanced thermal conductivity for Ag-deposited alumina sphere/epoxy resin composites through manipulating interfacial thermal resistance. *Compos. Part A: Appl. Sci. Manuf.* **2018**, *107*, 561–569.
[22] Gu, J. W.; Ruan, K. P. Breaking through bottlenecks for thermally conductive polymer composites: A perspective for intrinsic thermal conductivity, interfacial thermal resistance and theoretics. *Nano-Micro Lett.* **2021**, *13*, 110.
[23] Huang, X. Y.; Zhi, C. Y.; Lin, Y.; Bao, H.; Wu, G. N.; Jiang, P. K.; Mai, Y. W. Thermal conductivity of graphene-based polymer nanocomposites. *Mater. Sci. Eng. R: Rep.* **2020**, *142*, 100577.
[24] Wang, W. Y.; Ma, X.; Sun, D. X.; Qi, X. D.; Yang, J. H.; Wang, Y. Achieving electrical insulation, high thermal conductivity and high fracture toughness in polyamide 6/carbon nanofiber composites through the interfacial welding effect of elastomer. *Compos. Part A: Appl. Sci. Manuf.* **2020**, *128*, 105671.
[25] Kusunose, T.; Uno, Y.; Tanaka, Y.; Sekino, T. Isotropic enhancement of the thermal conductivity of polymer composites by dispersion of equiaxed polyhedral boron nitride fillers. *Compos. Sci. Technol.* **2021**, *208*, 108770.
[26] Qin, M. M.; Xu, Y. X.; Cao, R.; Feng, W.; Chen, L. Efficiently controlling the 3D thermal conductivity of a polymer nanocomposite via a hyperelastic double-continuous network of graphene and sponge. *Adv. Funct. Mater.* **2018**, *28*, 1805053.
[27] Han, C.; Ma, J.; He, H. W.; Yu, W. W.; Zhang, Y. C.; Cui, C.; Ma, Q. Y.; Jin, Y. S. Fabrication of curdlan connected honeycomb-like 3D BN-CNT network for enhancing the thermal conductivity of epoxy composites. *Chem. Eng. J.* **2025**, *507*, 160443.
[28] Ming, X.; Wei, A. R.; Liu, Y. J.; Peng, L.; Li, P.; Wang, J. Q.; Liu, S. P.; Fang, W. Z.; Wang, Z. Q.; Peng, H. Q. et al. 2D-topology-seeded graphitization for highly thermally conductive carbon fibers. *Adv. Mater.* **2022**, *34*, 2201867.
[29] Xin, G. Q.; Yao, T. K.; Sun, H. T.; Scott, S. M.; Shao, D. L.; Wang, G. K.; Lian, J. Highly thermally conductive and mechanically strong graphene fibers. *Science* **2015**, *349*, 1083–1087.
[30] Sun, J. Y.; Chen, Y. B.; Priydarshi, M. K.; Gao, T.; Song, X. J.; Zhang, Y. F.; Liu, Z. F. Graphene glass from direct CVD routes: Production and applications. *Adv. Mater.* **2016**, *28*, 10333–10339.
[31] Khan, A.; Islam, S. M.; Ahmed, S.; Kumar, R. R.; Habib, M. R.; Huang, K.; Hu, M.; Yu, X. G.; Yang, D. R. Direct CVD growth of graphene on technologically important dielectric and semiconducting substrates. *Adv. Sci.* **2018**, *5*, 1800050.
[32] Wang, Y. X.; Xu, N.; Li, D. Y.; Zhu, J. Thermal properties of two dimensional layered materials. *Adv. Funct. Mater.* **2017**, *27*, 1604134.
[33] Zhan, H. F.; Zhang, G.; Zhuang, X. Y.; Timon, R.; Gu, Y. T. Low interfacial thermal resistance between crossed ultra-thin carbon nanothreads. *Carbon* **2020**, *165*, 216–224.
[34] Zhang, F.; Sun, Y. X.; Guo, L.; Zhang, Y. H.; Liu, D.; Feng, W.; Shen, X.; Zheng, Q. B. Microstructural welding engineering of carbon nanotube/polydimethylsiloxane nanocomposites with improved interfacial thermal transport. *Adv. Funct. Mater.* **2024**, *34*, 2311906.
[35] Ding, D. L.; Huang, R. Y.; Peng, B.; Xie, Y. Y.; Nie, H. T.; Yang, C. H.; Zhang, Q. Y.; Zhang, X. A.; Qin, G. Z.; Chen, Y. H. Effect of nanoscale *in situ* interface welding on the macroscale thermal conductivity of insulating epoxy composites: A multiscale simulation investigation. *ACS Nano* **2023**, *17*, 19323–19337.